Half-Metal Spin-Gapless Semiconductor Junctions as a Route to the Ideal Diode

Ersoy Şaşıoğlu[1], Thorsten Aull[1], Dorothea Kutschabsky[1], Stefan Blügel[2], and Ingrid Mertig[1,3]
[1]*Institute of Physics, Martin Luther University Halle-Wittenberg, D-06120 Halle (Saale), Germany*
[2]*Peter Grünberg Institut and Institute for Advanced Simulation, Forschungszentrum Jülich and JARA, D-52425 Jülich, Germany*
[3]*Max Planck Institute of Microstructure Physics, Weinberg 2, D-06120 Halle (Saale), Germany*

The ideal diode is a theoretical concept that completely conducts the electric current under forward bias without any loss and that behaves like a perfect insulator under reverse bias. However, real diodes have a junction barrier that electrons have to overcome and thus they have a threshold voltage V_T, which must be supplied to the diode to turn it on. This threshold voltage gives rise to power dissipation in the form of heat and hence is an undesirable feature. In this work, based on half-metallic magnets (HMMs) and spin-gapless semiconductors (SGSs) we propose a diode concept that does not have a junction barrier and the operation principle of which relies on the spin-dependent transport properties of the HMM and SGS materials. We show that the HMM and SGS materials form an Ohmic contact under any finite forward bias, while for a reverse bias the current is blocked due to spin-dependent filtering of the electrons. Thus, the HMM-SGS junctions act as a diode with zero threshold voltage V_T, and linear current-voltage (I-V) characteristics as well as an infinite on:off ratio at zero temperature. However, at finite temperatures, non-spin-flip thermally excited high-energy electrons as well as low-energy spin-flip excitations can give rise to a leakage current and thus reduce the on:off ratio under a reverse bias. Furthermore, a zero threshold voltage allows one to detect extremely weak signals and due to the Ohmic HMM-SGS contact, the proposed diode has a much higher current drive capability and low resistance, which is advantageous compared to conventional semiconductor diodes. We employ the nonequilibrium Greens function method combined with density-functional theory to demonstrate the linear I-V characteristics of the proposed diode based on two-dimensional half-metallic Fe/MoS_2 and spin-gapless semiconducting VS_2 planar heterojunctions.

I. INTRODUCTION

A diode is a two-terminal device that conducts electric current in only one direction but restricts current from flowing in the opposite direction, i.e., it acts as a one-way switch for current. Diodes are also known as rectifiers because they change alternating current into direct current. Diodes are of several types, with different properties depending on the materials that they consist of [1–3]. For instance, p-n-junction diodes are formed by joining a p-type semiconductor with n-type semiconductor and they are the elementary building blocks of the three-terminal transistors. The Esaki diode (or tunnel diode) [4] is a heavily doped p-n-junction diode, in which the electron transport in the contact region is via quantum-mechanical tunneling under forward bias and it shows the negative-differential-resistance (NDR) effect (see Fig. 1), which allows it to function as oscillator and amplifier. In connection with the Esaki diode, when the doping concentration on the p side or n side is nearly or not quite degenerate, the current in the reverse direction is much larger than in the forward direction and hence such a device is called backward diode [1, 5, 6]. In contrast to semiconductor-semiconductor diodes, a Schottky-barrier diode [1] is formed by joining a metal with a n-type semiconductor. Compared to typical p-n junctions, Schottky diodes have very fast switching times and higher current drive capability.

Diodes are used for various applications, ranging from power conversion to overvoltage protection and from signal detection and mixing to switches. Due to the junction barrier, diodes have a threshold (or turn on) voltage V_T, which must be supplied to the diode for it to conduct any considerable forward current. In Fig. 1, we show the current-voltage (I-V) characteristics of the different types of diodes and compare them with the concepts of the ideal diode and the Ohmic junction. For p-n-junction (silicon) diodes the threshold voltage V_T is around 0.7 V, while for Schottky diodes V_T is between 0.2 V and 0.3 V. Backward diodes have zero threshold voltage but their on:off current ratios as well as their voltage-operation windows are rather small. The threshold voltage V_T gives rise to the power dissipation ($P = V_T \times I$) in the diode in the form of heat and hence it is an undesirable feature. The larger the value of V_T, the higher is the power dissipation.

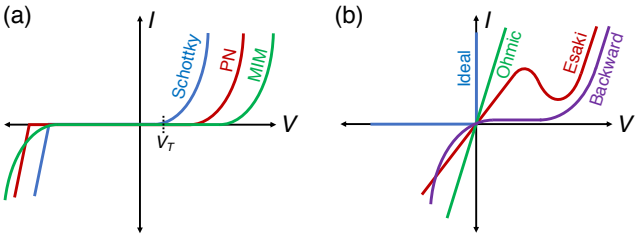

FIG. 1: (a) A schematic representation of the current-voltage (I-V) characteristics of the conventional three types of diodes [Schottky, p-n, and metal-insulator-metal (M-I-M) diodes]. (b) The I-V curves of an ideal diode, an Ohmic junction, an Esaki (tunnel diode), and a backward diode.

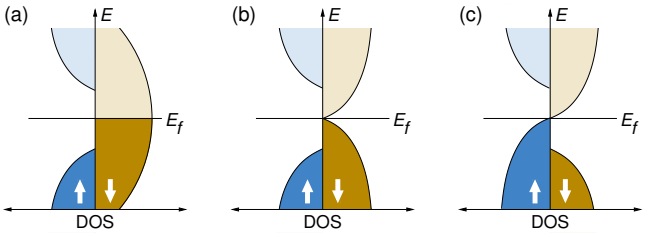

FIG. 2: A schematic representation of the density of states for (a) a half metallic magnet, (b) a type-I spin-gapless semiconductor, and (c) a type-II spin-gapless semiconductor.

Although the ideal diode is a theoretical concept, it has been suggested that superconductor-semiconductor junctions possess I-V characteristics that are similar to the ideal one under a forward bias [7]. Initial experiments by McColl *et al.* on a superconductor-semiconductor junction diode based on lead and p-type GaAs have shown ideal-diode behavior for forward applied voltages less than the superconducting-energy-gap parameter Δ. In this voltage window (a few millielectronvolts) the diode exhibits a high degree of nonlinearity in its I-V characteristics [7]. Superconductor-semiconductor junctions have subsequently been studied as the most sensitive detectors and mixers of microwaves [8–12]. However, in contrast to the Schottky diode behavior, superconductor-semiconductor junctions possess symmetric I-V curves with $I(-V) = -I(V)$, close to zero bias, giving rise to a relatively small on:off current ratio [12]. Furthermore, the operation temperature of such diodes is limited by the phase-transition temperature of superconductors, which is far below room temperature. Another type of diode that has a zero threshold voltage V_T is the so-called geometric diode, the operation principle of which relies on the geometric asymmetry of a conducting thin film [13–16]. Geometric diodes are ultra-fast ballistic transport devices, where the critical dimension of the device is comparable to the mean-free path length of the electrons. It was, however, been shown that geometric asymmetry of the diode alone cannot induce a current rectification and thus in addition to geometry, nonlinearity (high-order many-body interactions) is required to realize the geometric diode [17]. This also explains why the experimentally measured current rectification in graphene-related geometric diodes is very low [13, 14] as the non-linearity, i.e., electron-phonon interactions are rather weak in these systems.

For device applications, a special class of materials, the so-called spin-gapless semiconductors (SGSs), are receiving substantial attention. The concept of SGSs was proposed by Wang in 2008 [18, 19]. By employing first-principles calculations the author predicted SGS behavior in the Co-doped dilute magnetic semiconductor $PbPdO_2$. Subsequently, different classes of materials ranging from two dimensional (2D) to three dimensional (3D) have been predicted to possess SGS behavior and some of them have been confirmed experimentally. The SGSs lie on the border between magnetic semiconductors and half-metallic magnets (HMMs) [20]. A schematic density of states (DOS) of HMM and SGSs is shown in Fig 2. In SGSs, the mobility of charge carriers is essentially higher than in normal semiconductors, making them promising materials for nanoelectronic applications. Moreover, the spin-dependent transport properties of SGSs and HMMs lead to the emergence of device concepts in spintronics. Recently, a reconfigurable magnetic tunnel diode and transistor concept based on SGSs and HMMs has been proposed [21, 22]. The magnetic tunnel diode allows electrical current to pass either in one or the other direction, depending on the relative orientation of the magnetization of the HMM and SGS electrodes. Moreover, the proposed devices present tunnel magnetoresistance effect, allowing the combination of nonvolatility and reconfigurability on the diode (transistor) level, which is not achievable in semiconductor nanoelectronics.

In this paper, we propose a diode concept, based on a HMM and a SGS electrode, that we call Ohmic spin diode (OSD) and demonstrate proof of the principle by *ab-initio* quantum transport calculations. Analogous to the metal-semiconductor junction diode (the Schottky-barrier diode), HMM-SGS junctions act as a diode, the operation principle of which relies on the spin-dependent transport properties of the HMM and SGS materials. We show that HMM and SGS materials form an Ohmic contact under any finite forward bias, giving rise to linear current-voltage (I-V) characteristics, while for a reverse bias the current is blocked due to the filtering of the electrons. In contrast to the Schottky diode, the proposed diode does not require the doping of the SGS and also does not have a junction barrier and thus it has a zero threshold voltage V_T and an infinite on:off current ratio at zero temperature. However, at finite temperatures non-spin-flip thermally excited high-energy electrons as well as low-energy spin-flip excitations can give rise to leakage current and thus reduce the on:off ratio under a reverse bias. Moreover, due to the Ohmic HMM-SGS contact, the proposed diode has a much higher current drive capability and low resistance, which is advantageous compared to conventional semiconductor diodes. To demonstrate the linear I-V characteristics of the concept we construct a planar HMM-SGS junction based on 2D half-metallic Fe/MoS_2 and spin-gapless semiconducting VS_2 and employ the nonequilibrium Greens function method combined with density-functional theory (DFT). We find that at zero bias the VS_2 and Fe/MoS_2 electrodes couple ferromagnetically; however. this coupling changes sign from ferro- to antiferromagnetic for a critical forward bias voltage of $V = 180$ mV. The VS_2–Fe/MoS_2 junction diode possesses linear I-V characteristics for forward bias voltages up to $V = 180$ mV and a very small threshold voltage of $V_T = 30$ meV, which can be attributed to the minority-electron conduction-band minimum of the spin-gapless semiconducting VS_2 material. Moreover, we obtain a very high current density ($J = 2350$ μA/μm

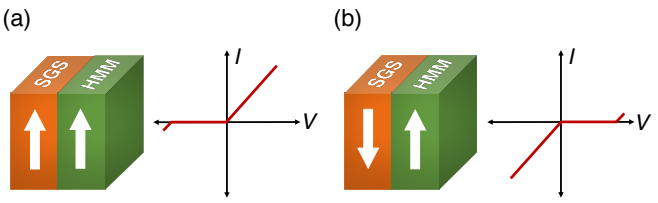

FIG. 3: (a) A schematic representation of the HMM-SGS junction for parallel orientation of the magnetization directions of the electrodes and the corresponding current-voltage (I-V) curves. (b) The same as (a) for antiparallel orientation of the magnetization directions of the electrodes. The white arrows indicate the direction of the magnetization of the electrodes.

for $V = 180$ mV), which makes the VS_2–Fe/MoS_2 OSD highly promising for low-temperature nanoelectronic applications.

II. HMM-SGS JUNCTIONS

The structure of the proposed OSD and its I-V characteristics are shown schematically in Fig. 3. Analogous to the metal-semiconductor Schottky-barrier diode, the OSD is composed of a HMM electrode and a type-II SGS electrode. Depending on the magnetization direction of the electrodes, the diode conducts current either under forward bias [Fig. 3(a), parallel orientation (ferromagnetic interelectrode coupling)] or under the reverse bias [Fig. 3(a), antiparallel orientation (antiferromagnetic interelectrode coupling)], similar to the case of the backward diode mentioned in Sec. I. In the presentation of the schematic I-V characteristics of the OSD in Fig. 3, we assume that HMM material possesses a gap in the spin-up channel around the Fermi level, while type-II SGS material has a gap in the spin-up (spin-down) channel above (below) the Fermi level, as shown schematically in Fig. 2. In type-II SGSs, the conduction- and valence-band edges of the different spin channels touch at the Fermi energy, while in type-I SGSs the spin-up (majority-spin) band looks like the on in HMMs but the difference is in the spin-down (minority-spin) band. The valence- and conduction-band edges are touching at the Fermi energy, so that a zero-width gap exists. One of the important advantages of type-I SGSs is that no energy is required for the excitation of the electrons from the valence to the conduction band and excited electrons or holes can be 100% spin-polarized like in HMMs. In construction of the OSD, the useo possible. of a type-I SGS instead of the HMM is als

The linear I-V characteristics of the OSD presented in Fig. 3(a) can be qualitatively explained on the basis of the schematic energy-band diagram shown in Fig. 4. If we assume that both HMM and SGS electrodes have the same work function and equal Fermi levels, then no charge transfer takes place between the electrodes. However, in real materials due to different work functions there might be a charge transfer from one material to another at the interface, which might give rise to band bending for the SGS. Besides this, due to interactions, junction materials might not retain their half metallic and spin-gapless semiconducting properties near the interface and hence the band diagram would not be as sharp as in Fig. 4. For the device configuration shown in Fig. 3(a) the relevant channel for the transport is the minority-spin (spin-down) channel, whereas the majority-spin (spin-up) channel is insulating due to the spin gap of HMM material on the right-hand side of the junction. In the spin-down channel, the HMM behaves like a normal metal with states below and above the Fermi energy, while the SGS electrode on the left-hand side behaves like a semiconductor (or insulator) but with a Fermi level touching the conduction-band minimum. Due to this electronic band structure of the SGS, in contrast to the Schottky diode, no energy barrier is formed at the interface between a HMM and a SGS material. Such a junction acts as an Ohmic contact under forward bias as shown in Fig. 4(b). In this case, the spin-down electrons from the occupied valence band of the HMM electrode can flow into the unoccupied conduction band of the SGS electrode without experiencing a potential barrier, while for a reverse bias the current is blocked due to the spin gap of HMM material [see Fig. 4(c)]. Note that under a forward bias, the current flowing through the OSD is 100% spin polarized. Note also that the same discussion applies in the case of antiparallel orientations of the magnetization directions of the electrodes [see Fig. 4(d), 4(e), and 4(f)].

As the HMM-SGS contact is Ohmic under a forward bias the current I through the diode varies linearly with the applied voltage V and the ratio V/I gives the combination of the interface (R_I) and series resistance (R_S) of the HMM and SGS materials ($V/I = R_I + R_S$). The resistance of SGS materials is usually much lower than that of conventional n- or p-type semiconductors [23] and thus the combination of low resistance with the Ohmic nature of the interface allows a much higher current drive capability of the proposed OSD. It is worth noting that diodes with low resistance are critical for the performance of high-speed electronic devices. Besides the higher current drive capability of the OSD, the threshold voltage V_T can be tuned by a proper choice of the SGS material. The value of V_T is set by the energy difference between the minority-spin conduction-band minimum and the Fermi level. In an ideal SGS, this difference is zero and thus $V_T = 0$. Note, however, that in type-II SGSs, the spin-gapless semiconducting properties are not protected by any symmetry and thus ideal SGS behavior can only arise if a free parameter – e.g. pressure, strain, or doping – is tuned to a specific value. A zero V_T allows one to detect extremely weak signals, even when no external bias circuit is used. Similar to the Schottky diode, the OSD is also a majority-carrier diode but it does not require doping and it will possess all the advantages of the Schottky diode, such as high operation frequencies,

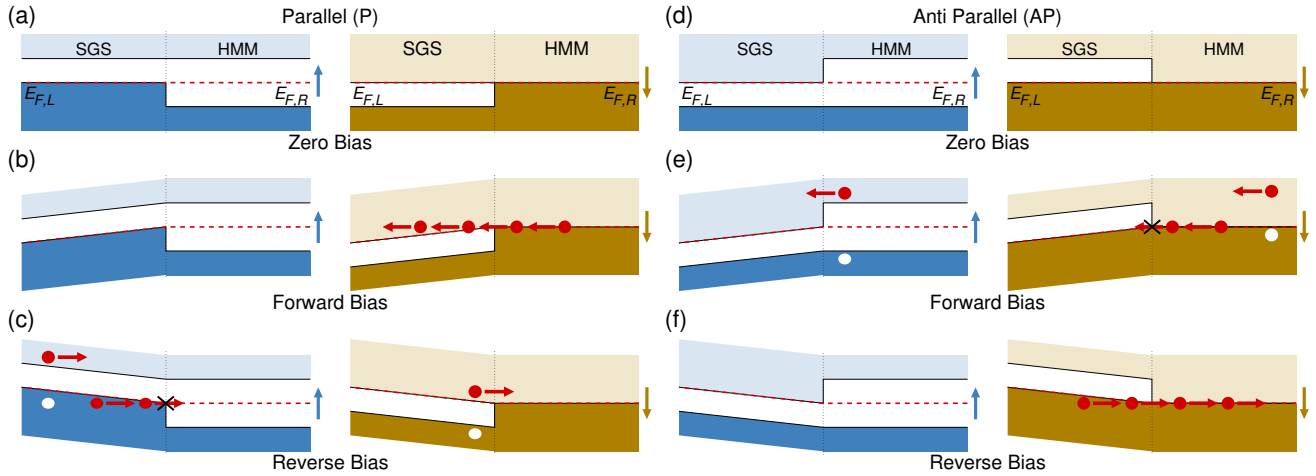

FIG. 4: A schematic representation of the band diagram and thermal (non-spin-flip) electron-hole excitations for spin-up and spin-down electrons for the SGS-HMM contact for parallel (P) orientation of the magnetization directions of the electrodes: (a) for zero bias, (b) for forward bias, and (c) for reverse bias. The Fermi level is denoted by red dashed line. (d)–(f) The same as (a)–(c) for the antiparallel (AP) orientations of the magnetization directions of the electrodes [see Figs. 3(a) and 3(b)].

low resistance and capacitance, etc. Note also that, in principle, a Schottky diode can be turned into an Ohmic contact by heavily doping the semiconductor electrode; however, in this case it loses its diode functionality.

Up to now, the discussion of the I-V characteristics of the OSD is based on the schematic band diagram at zero temperature and thus an infinite on:off current ratio can be achieved. However, at finite temperatures, thermally excited electrons and holes can significantly reduce the on:off ratio. At this point, it is important to note that in conventional metal-semiconductor Schottky diodes electrons flow from semiconductor to the metal electrode under a forward bias, whereas in the OSD shown in Fig. 3(a) the process is just the opposite, i.e, from the half-metal to the spin-gapless semiconductor. In the former case, the on-state current stems from the combination of thermionic emission over the Schottky barrier and tunnelling through the barrier [24–26]. A very detailed analysis of these processes and their relative contributions to the total forward (on-state) current in Schottky diodes can be found in Ref. 24. Similarly, under a reverse bias, both processes contribute to the leakage current in Schottky diodes, with a significant weight coming from the tunneling (or thermionic field emission), since in this case the height of the Schottky barrier is fixed and only a very small fraction of the thermally excited high-energy electrons, which are at the tail of the Fermi-Dirac distribution function, can pass over the barrier. By increasing the height of the Schottky barrier, the contribution of thermionic emission can be significantly reduced, as the Fermi-Dirac distribution function decays exponentially at high energies [see Fig. 3(a)]; however, the contribution of the tunneling through the barrier cannot be prevented and at the same time the threshold voltage V_T increases. In the OSD, the leakage current due to tunneling does not exist; however, thermally excited high-energy electrons contribute to the reverse current, similar to the case of Schottky diode. In Figs. 5(b) and 5(c), we show schematically the population of unoccupied states around the Fermi energy for a HMM and a type-II SGS. In a HMM, thermal population of the states obeys the Fermi-Dirac distribution, i.e., more states in the metallic spin-channel and very few states for the insulating spin-channel, as they are far from the Fermi level. However, the situation turns out to be slightly different in type-II SGSs, due to their band structure, i.e., only a small fraction of the electrons can be thermally excited due to the gap in both spin channels, somewhat similar to the case of intrinsic semiconductors. Consequently, the reverse bias current (or the leakage current) is mainly determined by the size of the band gaps in SGS and HMM electrodes and by a proper choice of the large band-gap materials, the on:off current ratio can be significantly increased in OSDs. In addition to thermal excitations, spin-flip pro-

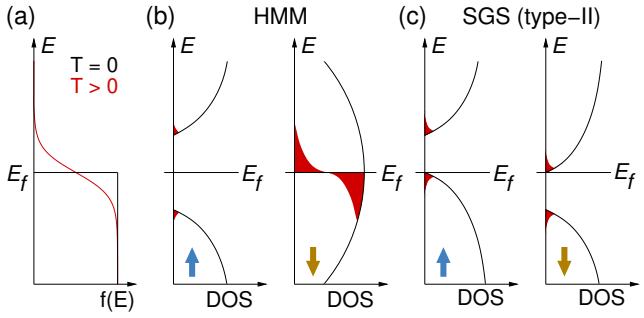

FIG. 5: (a) The Fermi-Dirac distribution for $T = 0$ K (black) and $T > 0$ K (red) and thermal population of states around the Fermi level for (b) a HMM and (c) type-II SGS. The occupied and unoccupied states above and below the Fermi level, respectively, are marked with a shaded red color.

TABLE I: The *I-V* characteristics of the OSD for parallel (P) and antiparallel (AP) orientations of the magnetization directions of the electrodes and all possible combinations of the spin character of the gaps in HMMs and SGSs. SGS ($\downarrow\uparrow$) indicates the spin channel where the gap exists below and above the Fermi level.

Spin gap	Orientation	Forward bias	Reverse bias
SGS ($\downarrow\uparrow$)/HMM ($\uparrow\uparrow$)	P	On	Off
SGS ($\downarrow\uparrow$)/HMM ($\uparrow\uparrow$)	AP	Off	On
SGS ($\downarrow\uparrow$)/HMM ($\downarrow\downarrow$)	P	Off	On
SGS ($\downarrow\uparrow$)/HMM ($\downarrow\downarrow$)	AP	On	Off
SGS ($\uparrow\downarrow$)/HMM ($\uparrow\uparrow$)	P	Off	On
SGS ($\uparrow\downarrow$)/HMM ($\uparrow\uparrow$)	AP	On	Off
SGS ($\uparrow\downarrow$)/HMM ($\downarrow\downarrow$)	P	On	Off
SGS ($\uparrow\downarrow$)/HMM ($\downarrow\downarrow$)	AP	Off	On

cesses can reduce the on:off current ratio and this will be discussed later.

In contrast to the Schottky diode, the spin degree of freedom provides a rich configuration space for the *I-V* curves of the OSD, which are determined by two parameters: (i) the magnetic coupling between electrodes, which allows the dynamical configuration of the diode in the case of antiferromagnetic interelectrode coupling via an external magnetic field; and (ii) the spin character of the gap in HMMs and SGSs. Depending on the magnetic coupling between electrodes, the OSD is in the on state either under forward bias (ferromagnetic interelectrode coupling or parallel orientation) or under reverse bias (antiferromagnetic interelectrode coupling or antiparallel orientation), as shown in Fig. 3. The second parameter, which plays a decisive role in determining the *I-V* characteristics of the OSD, is the spin-channel dependence of the gap in HMM and SGS electrodes. For instance, as mentioned above in the presentation of the schematic *I-V* characteristics of the OSD in Fig. 3, we assume that the HMM material has a gap in the spin-up channel and the SGS material has gaps in the spin-down (below E_F) and spin-up channels (above E_F). Although all known type-II SGSs possess an electronic band structure similar to that in Fig. 2(c), there are many HMMs, such as Heusler alloys, with a gap in the spin-down channel and OSD diodes constructed from such materials might have a different current direction than the present case. For completeness, in Table I we present the *I-V* characteristics of the OSD by taking into account both magnetic configurations of the electrodes and all possible combinations of the spin character of the gaps in HMMs and SGSs.

As the OSD is comprised of magnetic materials, its operation temperature is limited by the Curie temperature T_C of the constituent materials and thus for realization of the OSD, HMMs and SGSs with high T_C values are required. Two-dimensional transition-metal dichalcogenides [27–30] and 3D quaternary Heusler compounds [31–36] offer a unique platform to design, within the same family of compounds, HMMs and SGSs with high T_C values and similar lattice parameters and compositions, which allow coherent growth of these materials on top of each other. Besides high T_C values, large spin gaps in HMMs and SGSs are crucial to achieve high on:off current ratio in the OSD. In recent years, 2D transition-metal dichalcogenides have received significant experimental and theoretical interest, as they present unique electronic, optical, mechanical, and magnetic properties, thus holding great promise for a wide range device applications. Devices ranging from vertical tunnel diodes to vertical and lateral tunnel field-effect transistors (TFETs) have been experimentally demonstrated [37–44]. In particular, 2D lateral heterojunctions have opened up a direction in materials science and device applications [45]. TFETs based on 2D material heterojunctions (WTe_2-MoS_2, $MoTe_2$-MoS_2) have been reported to exhibit subthreshold slope below 5 mV/dec and high $I_{\rm ON}/I_{\rm OFF}$ ratios (approximately 10^8) at a low drain bias of 0.3 V, making them ideal candidates for ultralow-power computing [46].

Among the 2D transition-metal dichalcogenides, *V*-based compounds (VS_2, VSe_2, VTe_2) have attracted particular interest due to their intrinsic ferromagnetism. These compounds can crystallize in two different structures: the $1H$ phase and the $1T$ phase. The former phase is energetically more stable and possesses a SGS ground state [47, 48]. Although, theoretically, both $1H$ and $1T$ phases of *V*-based 2D compounds have been predicted to show ferromagnetism [49], experimentally the ferromagnetism has, however, only been observed in the $1T$ phase of VS_2 [50] and VSe_2 [51]. Note that the $1T$ phase of VSe_2 does not present SGS behavior; it is a normal ferromagnetic metal. However, in the one-monolayer limit, several 2D transition-metal dichalcogenides can adopt either a $1T$ or a $1H$ structure depending on the growth conditions [52]. It is very likely that VS_2 can also be grown in a $1H$ structure.

III. COMPUTATIONAL METHOD

Ground state electronic structure calculations are carried out using density functional theory (DFT), implemented in the QuantumATK P-2019.03 package [53]. We use the generalized-gradient-approximation (GGA)–Perdew-Burke-Ernzerhof (PBE) exchange-correlation functional [54] together with PseudoDojo pseudopotentials [55] and LCAO basis-sets. A dense $24 \times 24 \times 1$ **k**-point grid and density mesh cutoff of 120 hartree are used. To prevent interactions between the periodically repeated images, 20 Å of vacuum are added and Dirichlet and Neumann boundary conditions are employed. The electron temperature is set to 10 K. The total energy and forces converge to at least to 10^{-4} eV and 0.01 eV/Å, respectively. In order to estimate magnetic anisotropy energy, we employ the magnetic force theorem, including spin-orbit coupling [56].

The transport calculations are performed using

DFT combined with the nonequilibrium Green's function method (NEGF). We use a $24 \times 1 \times 172$ **k**-point grid in self-consistent DFT-NEGF calculations. The *I-V* characteristics were calculated within a Landauer approach [57], where $I(V) = \frac{2e}{h}\sum_\sigma \int T^\sigma(E,V)\,[f_L(E,V) - f_R(E,V)]\,\mathrm{d}E$. Here, V denotes the bias voltage, $T^\sigma(E,V)$ is the spin-dependent transmission coefficient for an electron with spin σ, and $f_L(E,V)$ and $f_R(E,V)$ are the Fermi-Dirac distributions of the left and right electrodes, respectively. The transmission coefficient $T^\sigma(E,V)$ is calculated using a 300×1 **k**-point grid.

IV. RESULTS AND DISCUSSION

The OSD concept introduced in Sec. II can be realized either by using 3D Heusler compounds or 2D transition-metal dichalcogenides. In the following, due to their structural simplicity we focus on the 2D materials and demonstrate the proof of principle by *ab-initio* quantum transport calculations. As the electrode materials of the OSD, we choose VS_2 and Fe/MoS_2. The former is an intrinsic ferromagnet with spin-gapless semiconducting behavior in the monolayer $1H$ phase, while the half-metallic ferromagnetism in the latter Fe/MoS_2 material is achieved by functionalization of the $1H$ semiconducting MoS_2. Based on first-principles calculations, Jiang *et al.* [58] have shown that deposition of the Fe atoms on MoS_2 gives rise to the 2D half-metallic ferromagnetism with a relatively high T_C value of 465 K and a large spin gap, which makes the Fe/MoS_2 a promising material for spintronic and nanoelectronic applications.

Since the electronic and magnetic as well as structural properties of both electrode materials have been extensively discussed in the literature, in the following we will briefly overview their basic properties, which will be necessary in order to understand the transport characteristics of the OSD. In Table II, we present the optimized lattice constants and the total magnetic moments as well as the magnetic anisotropy energies for the $1H$ phase of VS_2 and Fe/MoS_2. Our ground-state calculations for both materials are in good agreement with previous published data. In particular, similar lattice parameters and compositions, as well as the same $1H$ phase, of the two materials are crucial for realization of the planar VS_2-Fe/MoS_2 heterojunctions. VS_2 has a relatively simple band structure, shown in Fig. 6(b), where the exchange splitting of the V-3*d* (predominantly d_{z^2}) bands around the Fermi energy is responsible for its spin-gapless semiconducting nature and thus it has a magnetic moment of 1 μ_B, carried by the V atom. Furthermore, VS_2 is not a perfect SGS; it has a very small indirect band gap of 50 meV, i.e., the valence-band maximum and conduction-band minimum are at around 20 meV and 30 meV, respectively. The former plays a decisive role in determining the threshold voltage V_T of the OSD in the case of ferromagnetic coupling of the VS_2 and Fe/MoS_2 electrodes, while the latter plays the same role in the case of antiferromagnetic coupling. Note that in the present OSD based on a planar VS_2-Fe/MoS_2 heterostructure, the coupling between the electrodes is ferromagnetic, as is discussed later. On the other hand, the Fe-deposited MoS_2 turns into a half-metallic magnet with a gap of about 1 eV in the spin-up channel and with a total magnetic moment of 2 μ_B, which is localized on the Fe atom. Note that PBE is well know to underestimate the band gap of semiconductors compared to the more accurate *GW* approach. However, the situation is different for 2D SGSs, since the application of *GW* method for the similar material VSe_2 reduces the band gap from 250 meV (PBE) to 170 meV [29]. We expect a similar behavior for the VS_2 compound when the *GW* method is employed. Also, spin-orbit coupling has a negligible effect on the spin polarization of both materials and thus it is not taken into account in our device calculations .

TABLE II: The calculated lattice parameter a, total magnetic moment m_T, magnetic anisotropy energy K (per formula unit), and the work-function ϕ for VS_2 and Fe/MoS_2. The values of the Curie temperature T_c are taken from the literature.

Compound	a (Å)	m_T (μ_B)	K (meV)	ϕ (eV)	T_C (K)
VS_2	3.174	1.00	0.20	5.71	138 [49]
Fe/MoS_2	3.175	2.00	0.42	4.72	465 [58]

In Fig. 6(a), we show the atomic structure of the OSD, which is formed by joining one monolayer of VS_2 (left electrode) and one monolayer of Fe/MoS_2 (right electrode) laterally in a single plane. Due to the almost identical lattice parameters of both materials, as well as their similar compositions, they form a perfect interface. We assume periodicity of the device in the x-direction. The z-direction is chosen as the transport direction. The total length of the scattering region is about 115.5 Å, which consists of 77 Å VS_2 and 38.5 Å Fe/MoS_2. The length of the former electrode is chosen larger because of the longer screening length in SGSs.

When the half metallic Fe/MoS_2 makes contact with VS_2, free electrons will flow from the half-metallic Fe/MoS_2 side to the spin-gapless semiconducting VS_2 side, because the work function of the Fe/MoS_2 is smaller than that of VS_2 (see Table II). Note that the work function of the SGS VS_2 is defined in the same way as in metals, i.e., the energy difference between the vacuum level and the Fermi energy E_F. When the charge redistribution reaches the equilibrium, near the interface region the Fe/MoS_2 will be positively charged, whereas the VS_2 will be negatively charged. Thus, an electric dipole will be induced at the interface region. Such a charge redistribution influences the electronic and magnetic properties of the materials near the interface, as seen in the zero-bias projected device density of states (DDOS) shown in Fig. 7. Near the interface, charge transfer takes place

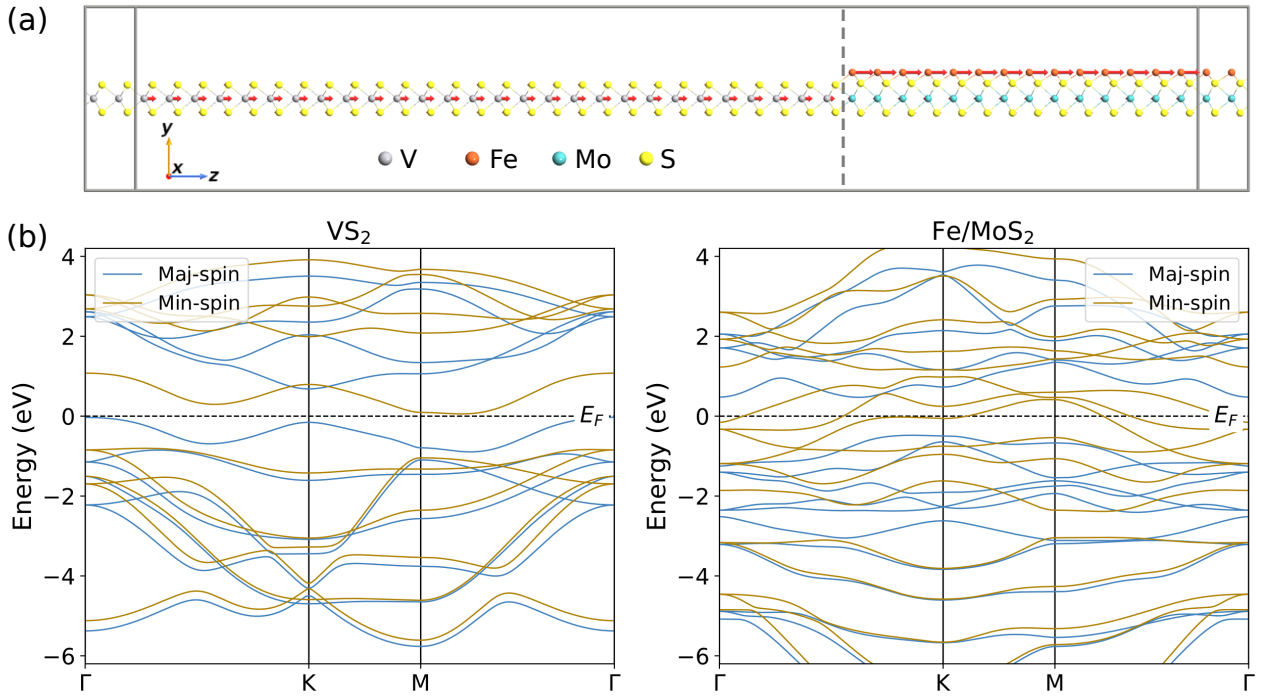

FIG. 6: (a) The atomic structure of the VS_2-Fe/MoS_2 Ohmic spin diode. The arrows show the magnetic moments of V and Fe atoms in the SGS and HMM electrodes within the scattering region. The size of the arrows is proportional to the magnitude of the magnetic moments. The system is periodic in the x-direction in the plane orthogonal to the magnetization direction, which is also the transport direction. The vertikal dashed lines denote the interface. (b) The calculated spin-resolved bulk electronic band structure along the high-symmetry lines in the Brillouin zone for VS_2 (left-hand panel) and Fe/MoS_2 (right-hand panel). For both compounds, the dashed lines denote the Fermi energy, which is set to zero.

within the spin-down channel and thus the magnetic moment of the Fe atoms increases towards the interface, i.e., 2.15 $\mu_B \rightarrow$ 2.17 $\mu_B \rightarrow$ 2.56 μ_B, as shown by the arrows in Fig. 6(a), where the size of the arrows is proportional to the magnitude of the magnetic moments. The transferred charge occupies the spin-down channel on the VS_2 side by creating interface states, which can be clearly seen on the projected DDOS shown in Fig. 7 and as a consequence the magnetic moment of the V atoms at the interface and subinterface lines is reduced from its bulk value of 1.13 μ_B to 0.53 μ_B and 0.95 μ_B, respectively. As can be seen, the influenced region is rather small, being within four atomic lines and restricted to the spin-down channel. The change in the spin-up channel is more or less negligible.

Long-range magnetic order is prohibited in the 2D magnets at finite temperatures due to the Mermin-Wagner theorem [59]. However, this restriction can be removed by magnetic anisotropy and it enables the occurrence of 2D magnetic order at finite temperatures. For both materials, we have calculated magnetic anisotropy energies K, which are presented in Table II. Both materials have an in-plane magnetization with K values of 0.2 meV (VS_2) and 0.42 meV (Fe/MoS_2). However, magnetic anisotropy within the plane for VS_2 is negligibly small (a few nanoelectronvolts), while for Fe/MoS_2 it is around 5 μeV, which is large enough for a finite-temperature magnetic order. The negligible value of K for VS_2 implies the lack of finite-temperature magnetic order by virtue of the Mermin-Wagner theorem. However, room-temperature ferromagnetism has been experimentally detected in similar materials such as VSe_2 [51], which has also negligible in-plane magnetic anisotropy, and the origin of the long-range ferromagnetic order is attributed to the finite-size effects [60, 61]. However, in VS_2-Fe/MoS_2 junction, the Fe/MoS_2 acts as a pinning electrode, which introduces a preferred in-plane magnetic orientation in the VS_2 electrode via the ferromagnetic interelectrode coupling. Our calculations show that ferromagnetic interelectrode coupling is preferable compared to antiferromagnetic interelectrode coupling and that the energy difference between the two configurations is about 22 meV.

Besides the magnetic anisotropy energy K and the interelectrode coupling, another important parameter for the realization of the OSD is the Curie temperature T_C of the constituent materials. The T_C values for both materials have been estimated from first principles in Refs 49 and 58 (see Table II). The T_C value of Fe/MoS_2 is higher than room temperature, while for VS_2 (T_C = 139 K) is below room temperature. Nevertheless, such a value is high enough for an experimental demonstration of the

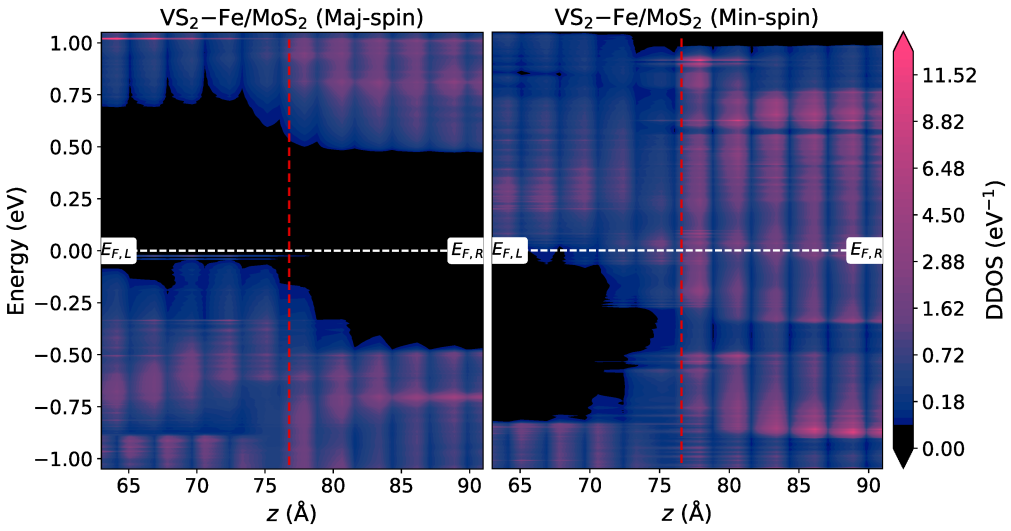

FIG. 7: The zero-bias projected device density of states (DDOS) for the majority (left hand panel) and minority (right hand panel) electrons for the Ohmic spin diode around the interface (see Fig. 6 for the atomic structure of the OSD). The horizontal white dashed lines indicate the Fermi level. The vertical red dashed lines denote the interface.

device.

Next, we discuss the electronic and transport properties of the OSD under a finite bias voltage. As mentioned above, although at zero bias the coupling between the SGS and HMM electrodes is ferromagnetic, we find that this coupling changes sign from ferromagnetic to antiferromagnetic under a forward bias of about 180 mV. Note that electric field or voltage control of magnetism on the nanoscale is highly appealing for the development of nanoelectronic devices with low power consumption [62–64]. A voltage-induced interlayer exchange coupling in magnetic tunnel junctions has been discussed theoretically via high-voltage tunneling [65–67] and has been experimentally demonstrated via mobile oxygen vacancies [68]. A sign change in magnetic coupling with the bias voltage allows the realization of devices with unique functionalities, which will be considered in a separate paper. In Figs. 8(a) and 8(b), we show the spin-resolved projected DDOS for bias voltage of 0.3 V (forward bias) and -0.3 V (reverse bias), respectively. Note that for the purpose of the demonstration of the OSD concept, we constrain the magnetic coupling between electrodes to the ferromagnetic state (parallel orientation) in the VS_2-Fe/MoS_2 junction for bias voltages higher than 180 mV. As one can see, for a forward bias, the spin-gapless and the half-metallic behavior is more or less preserved at the interface for both spin channels. Just a few new states arise at the interface in the spin-up channel, this being due to antiferromagnetic coupling of the single V atom at the interface. The interface V atom possesses a magnetic moment of -0.55 μ_B and variation of the magnetic moments in Fe and other V atoms near the interface is also negligible.

On the other hand, for a reverse bias the coupling between electrodes remains ferromagnetic and thus the electronic and magnetic structure near the interface is similar to the zero-bias case with the exception of the band bending in the VS_2 electrode, which take places near the interface region, within the 40 Å. Note that the band bending is not linear due to charge transfer as well as the complex metallic screening of the Fe/MoS_2 electrode. Indeed, we observe a flat region of about 15 Å on the projected DDOS [see Fig. 8(b)] of the junction on the VS_2 side and then potential drops more or less linearly with distance.

The I-V characteristics of the VS_2-Fe/MoS_2 OSD can be qualitatively explained on the basis of the projected DDOS shown in Fig. 8. For a forward bias, the OSD is in the on-state, i.e., minority-spin electrons from the occupied states of the Fe/MoS_2 electrode can flow into the unoccupied states of the VS_2 electrode due to the Ohmic contact and thus the transmission coefficient takes finite values within the bias window, as shown in middle panel of Fig. 8(a). Meanwhile, for majority-spin electrons the transmission coefficient is zero because both Fe/MoS_2 and VS_2 have no states within the voltage window. Thus the on-state current of the OSD is 100% spin polarized. On the other hand, for a reverse bias voltage, no current flows through the OSD since the energy gap in the majority spin channel of the Fe/MoS_2 electrode prevents the flow of the spin-up electrons from VS_2 electrode into the Fe/MoS_2 [see Fig. 8(b) left-hand panel], giving rise to a zero transmission coefficient. Similarly, the transmission coefficient for the spin-down channel is also zero due to the energy gap in the VS_2 electrode below the Fermi level.

Fig. 9 shows the calculated I-V characteristics of the VS_2-Fe/MoS_2 OSD at zero temperature. In the on-state, the current increases linearly with the applied bias and reaches 2350 μA/μm for a bias voltage of 180 mV, which is the maximum bias voltage at which ferromagnetic coupling between electrodes is retained. The VS_2-Fe/MoS_2 diode possesses a very small threshold voltage of about 30 mV, stemming from the indirect band gap of the SGS VS_2 electrode, which has a conduction-band minimum of 30 meV [see Fig. 6(b)] as discussed before. For bias

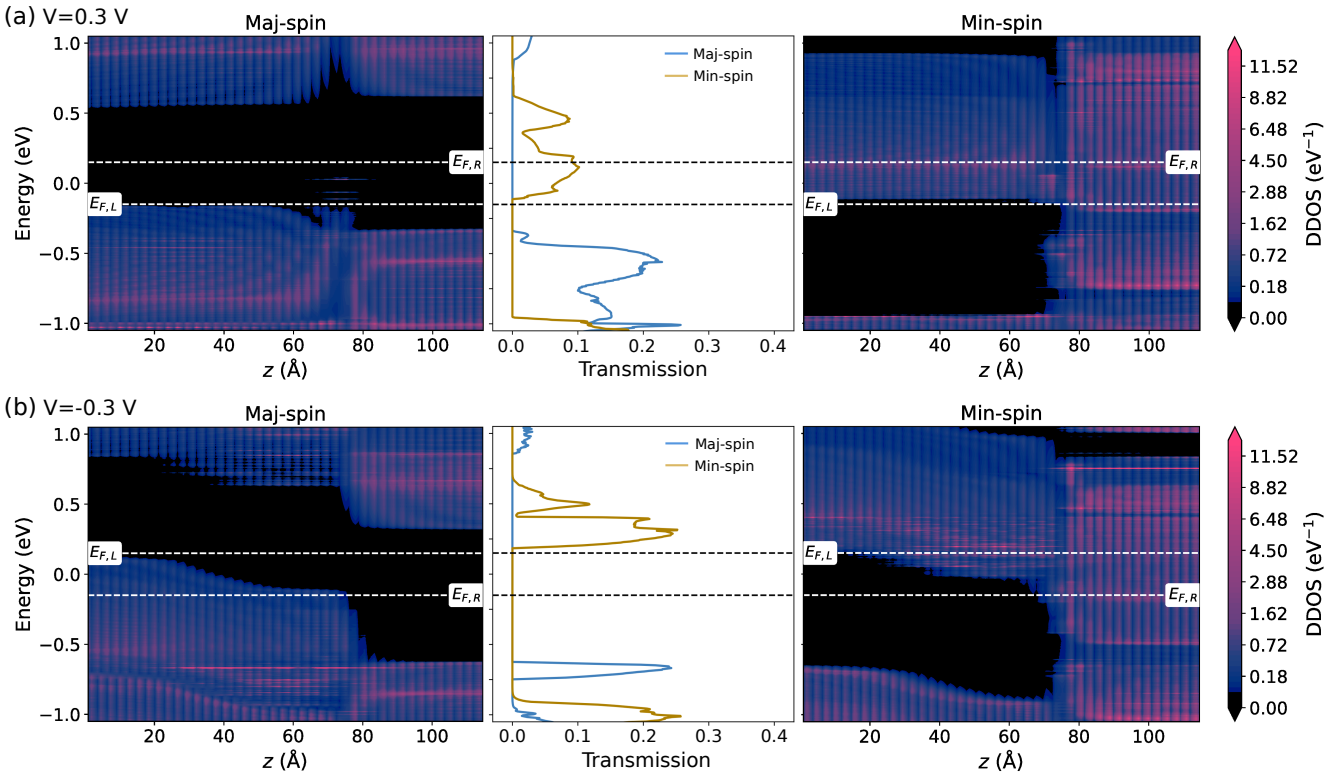

FIG. 8: (a) The projected device density of states (DDOS) for the majority (left-hand panel) and minority (right-hand panel) electrons for the VS_2-Fe/MoS_2 Ohmic spin diode (see Fig. 6 for the atomic structure of the Ohmic spin diode) under a positive voltage of $V = 0.3$ V. The middle panel shows the calculated transmission spectrum for the majority and minority electrons for the same applied voltage of $V = 0.3$ V. The upper and lower white (black) dashed lines indicate the Fermi level of the SGS and HMM electrodes. (b) The same as (a) for a negative voltage of $V = -0.3$ V.

voltages larger than the 180 mV, the I-V curve of the OSD takes a plateau shape, i.e., the current first monotonically increases up to 250 mV and then it starts to decrease. Such behavior can be attributed to the antiferromagnetic coupling of a single V atom at the interface, which now has a gap in the spin-down channel above the Fermi energy, in contrast to the rest of the atoms in the junction. This energy gap acts as a small potential barrier, giving rise to more reflection of the electrons, and thus it reduces the transmission. Furthermore, in the bias-voltage range from 180 mV to 300 mV, the magnetic moment of the V atom at the interface increases from -0.2 μ_B to -0.55 μ_B, which also explains the plateaulike shape of the I-V curve at higher voltages.

A feature of the proposed VS_2–Fe/MoS_2 OSD is that it has much higher current-drive capability, i.e., in the on state, for a bias voltage of $V = 180$ mV the calculated current density turns out to be around $I = 2350\ \mu A/\mu m$. This value is much higher than the on-state current density of devices based on 2D semiconducting materials [69] and lies far above the International Roadmap for Devices and Systems (IRDS) [69, 70] requirement ($1350\ \mu A/\mu m$). A negligible turn-on voltage $V_T = 30$ mV allows us to detect extremely weak signals and thus the OSD might find potential applications in antenna-coupled diode solar cells [71–73]. Besides this, the VS_2-Fe/MoS_2 OSD possesses an infinite on:off current ratio at zero temperature. However, as we discussed in Sec. II, thermally excited high-energy electrons would reduce the on:off current ratio to finite values. In the Landauer formalism of electronic current, the temperature effects can be taken into account via the Fermi-Dirac distribution function of the left $[f_L(E,V,T)]$ and right $[f_R(E,V,T)]$ electrodes (see Ref. [24] and thus the on:off current ratio can be caluclated for a given temperature T. However, this standard treatment should be modified for SGS materials due to their electronic band structure, which is discussed in Sec. II. Specifically, each spin channel of the SGS material with a proper population of the states above and below the Fermi energy should be taken into account. Since this modification has not been implemented in the current version of the QuantumATK package, we present the I-V characteristics only for zero temperature in Fig. 9.

As mentioned in Sec. II, the spin degree of freedom brings a certain functionality to the OSD, which can be dynamically configured by an external magnetic field; thus the OSD can be used as a switch. However, this is possible only for the OSDs having electrodes that cou-

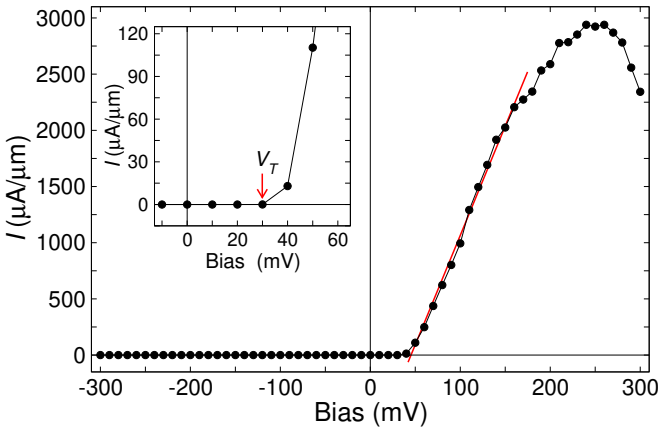

FIG. 9: The calculated current-voltage (I-V) characteristics of the VS_2-Fe/MoS_2 Ohmic spin diode. The red line shows the Ohmic behavior in the voltage range between 40 mV and 180 mV. The inset shows an enlargement of the range between -10 mV to 60 mV, to specify the threshold voltage V_T.

ple antiferromagnetically (the AP orientation). So in this case, in reversing the magnetization direction of one electrode from the antiparallel to the parallel orientation, the OSD switches from the on state to the off state like a transistor. This switching can be easily understood with the help of the schematic band diagram shown in Fig. 4 and will not be discussed here. The situation is even more interesting in the case of VS_2–Fe/MoS_2 OSD, i.e., in addition to the voltage-induced switching from the on state to the off state at around $V = 180$ mV, the OSD can again be switched back to the on state by a weak external magnetic field, making the VS_2–Fe/MoS_2 OSD highly appealing for nanoelectronic applications.

Finally, we would like to comment on the effect of low-energy spin excitations on the I-V characteristics of the VS_2-Fe/MoS_2 OSD. Apart from the high-energy thermal (non-spin-flip) excitations that we discuss in Sec. II, the temperature affects the electronic and magnetic structure of the VS_2 and Fe/MoS_2 via spin-dependent excitations, i.e., Stoner excitation and collective spin waves or magnons. In type-II SGSs such as VS_2, electrons can be excited from the majority-spin channel to the minority-spin channel via spin flip with almost vanishing energy [see Fig. 2(c)]. These excitations are known as single-particle Stoner excitations. They can populate the unoccupied minority-spin channel of VS_2 just above the Fermi energy. However, in VS_2, Stoner excitations require a large momentum transfer, since valance-band maximum and conduction-band minimum are at different $\mathbf{k}$ points in the Brillouin zone. The former is at the Γ point, while the latter is close to the M point [for the band structure of VS_2, see Fig. 6(b)] and thus single-particle spin-flip excitation requires a large momentum transfer and takes place at high temperatures close to the Curie temperature T_C. Nevertheless, they can populate the unoccupied minority channel above the Fermi energy and give rise to the leakage current under a revers bias [see Fig. 4(c)]. Moreover, the on:off current ratio will be further reduced. On the other hand, in half-metallic Fe/MoS_2, Stoner excitations are not allowed due to the existence of the spin gap; however, at finite temperatures, electron-magnon interaction can give rise to the appearance of nonquasiparticle states within the half-metallic gap just above the Fermi energy [74]. Thus, such states can reduce the spin polarization of the half metallic Fe/MoS_2 and affect its transport properties. Lastly, in addition to non-spin-flip as well as spin-flip excitations, defects at the interface, which destroy the SGS or HMM behavior can also reduce the on:off current ratio of the OSD.

V. CONCLUSIONS

In conclusion, we proposed a diode concept, which we call the OSD, based on SGS and HMM materials. Analogous to the metal-semiconductor junction diode (the Schottky-barrier diode), HMM-SGS junctions act as a diode the operation principle of which relies on the spin-dependent transport properties of the constituent HMM and SGS materials. We show that the HMM and SGS materials form an Ohmic contact under any finite forward bias voltage, giving rise to linear I-V characteristics, while for a reverse bias the current is blocked due to spin-dependent filtering of the electrons. In contrast to the Schottky diode, the proposed OSD does not require doping of the SGS electrode and it also does not have a junction barrier; thus it has a zero threshold voltage V_T and an infinite on:off current ratio at zero temperature. However, at finite temperatures, non-spin-flip thermally excited high-energy electrons as well as low-energy spin-flip excitations can give rise to a leakage current and thus reduce the on:off ratio under a reverse bias. As the leakage current is mainly determined by the size of the band gaps in SGS and HMM electrodes and by a proper choice of large band-gap materials, the on:off current ratio can be significantly increased in OSDs. Moreover, the spin degree of freedom provides a rich configuration space for the I-V characteristics of the OSD, which are determined by two parameters: (i) the spin character of the gap in HMM and SGS; and (ii) the magnetic coupling between electrodes, which allows the dynamical configuration of the diode in the case of antiferromagnetic coupling (antiparallel orientation) via an external magnetic field. We show that depending on the magnetic coupling between electrodes, the OSD is in the on state either under forward bias (parallel orientation) or under reverse bias (antiparallel orientation).

By employing the NEGF method combined with DFT, we demonstrate the rectification characteristics of the proposed OSD based on 2D half metallic Fe/MoS_2 and spin-gapless semiconducting VS_2 planar heterojunctions. We find that the VS_2Fe/MoS_2 junction diode possesses linear I-V characteristics for forward bias voltages up to 180 mV and that a bias voltage-induced ferromagnetic to antiferromagnetic interelectrode coupling then takes

place. Such a sign change in magnetic coupling with bias voltage allows the realization of devices with unique functionalities, which will be considered in a separate paper. Moreover, the VS_2Fe/MoS_2 OSD has a much higher current-drive capability ($I = 2350\ \mu A/\mu m$) and a very small threshold voltage of $V_T = 30$ mV, which allows us to detect extremely weak signals; thus it might find potential applications in antenna-coupled diode solar cells. We expect that our results will pave the way for experimentalists to fabricate the OSD based on 2D materials.

Acknowledgments

E.Ş and I.M. acknowledge support from *Sonderforschungsbereich* TRR 227 of the Deutsche Forschungsgemeinschaft (DFG) and funding provided by the European Union (EFRE), Grant No: ZS/2016/06/79307.

E.Ş and T.A. contributed equally to this work.

[1] S. M. Sze and K. K. Ng, *Physics of Semiconductor Devices* (John Wiley & Sons, Hoboken, 2007), 3rd ed.
[2] U. K. Mishra and J. Singh, *Semiconductor Device Physics and Design* (Springer Science & Business Media, Dordrecht, 2008).
[3] J.-P. Colinge and C. A. Colinge, *Physics of Semiconductor Devices* (Springer Science & Business Media, New York, 2006).
[4] L. Esaki, Phys. Rev. **109**, 603 (1958).
[5] X. Liu, D. Qu, H.-M. Li, I. Moon, F. Ahmed, C. Kim, M. Lee, Y. Choi, J. H. Cho, J. C. Hone, et al., ACS Nano **11**, 9143 (2017).
[6] K. Murali, M. Dandu, S. Das, and K. Majumdar, ACS Appl. Mater. Interfaces **10**, 5657 (2018).
[7] M. McColl, M. F. Millea, and A. H. Silver, Appl. Phys. Lett. **23**, 263 (1973).
[8] M. McColl, R. J. Pedersen, M. F. Bottjer, M. F. Millea, A. H. Silver, and F. L. V. Jr., Appl. Phys. Lett. **28**, 159 (1976).
[9] A. W. Kleinsasser, T. N. Jackson, D. McInturff, F. Rammo, G. D. Pettit, and J. M. Woodall, Appl. Phys. Lett. **57**, 1811 (1990).
[10] A. W. Kleinsasser and A. Kastalsky, Phys. Rev. B **47**, 8361 (1993).
[11] S.-T. Lo, K. Y. Chen, S.-D. Lin, J.-Y. Wu, T. L. Lin, M. R. Yeh, T.-M. Chen, and C.-T. Liang, Sci. Rep. **3**, 2274 (2013).
[12] D. Panna, K. Balasubramanian, S. Bouscher, Y. Wang, P. Yu, X. Chen, and A. Hayat, Sci. Rep. **8**, 5597 (2018).
[13] Z. Zhu, S. Joshi, S. Grover, and G. Moddel, J. Phys. D: Appl. Phys. **46**, 185101 (2013).
[14] Z. Zhu, S. Joshi, and G. Moddel, IEEE J. Sel. Top. Quantum Electron. **20**, 70 (2014).
[15] G. Auton, D. B. But, J. Zhang, E. Hill, D. Coquillat, C. Consejo, P. Nouvel, W. Knap, L. Varani, F. Teppe, et al., Nano Lett. **17**, 7015 (2017).
[16] T. Kang, R. J.-Y. Kim, G. Choi, J. Lee, H. Park, H. Jeon, C.-H. Park, and D.-S. Kim, Nat. Commun. **9**, 4914 (2018).
[17] N. Li and J. Ren, Sci. Rep. **4**, 6228 (2014).
[18] X. L. Wang, Phys. Rev. Lett. **100**, 156404 (2008).
[19] X. Wang, G. Peleckis, C. Zhang, H. Kimura, and S. Dou, Adv. Mater. **21**, 2196 (2009).
[20] R. A. De Groot, F. M. Mueller, P. G. Van Engen, and K. H. J. Buschow, Phys. Rev. Lett. **50**, 2024 (1983).
[21] E. Şaşıoğlu and S. Blügel, *Magnetic tunnel diode and magnetic tunnel transistor* (2016), Patent US20180309047A1, URL `https://patents.google.com/patent/US20180309047A1/en`.
[22] E. Şaşıoğlu, S. Blügel, and I. Mertig, Appl. Electron. Mater. **1**, 1552 (2019).
[23] S. Ouardi, G. H. Fecher, C. Felser, and J. Kübler, Phys. Rev. Lett. **110**, 100401 (2013).
[24] D. Stradi, U. Martinez, A. Blom, M. Brandbyge, and K. Stokbro, Phys. Rev. B **93**, 155302 (2016).
[25] H. Zhang, E. J. Miller, and E. T. Yu, J. Appl. Phys. **99**, 023703 (2006).
[26] A. Latreche, SN Appl. Sci. **1**, 188 (2019).
[27] M. Xu, T. Liang, M. Shi, and H. Chen, Chem. Rev. **113**, 3766 (2013).
[28] N. Mounet, M. Gibertini, P. Schwaller, D. Campi, A. Merkys, A. Marrazzo, T. Sohier, I. E. Castelli, A. Cepellotti, G. Pizzi, et al., Nat. Nanotechnol. **13**, 246 (2018).
[29] S. Haastrup, M. Strange, M. Pandey, T. Deilmann, P. S. Schmidt, N. F. Hinsche, M. N. Gjerding, D. Torelli, P. M. Larsen, A. C. Riis-Jensen, et al., 2D Mater. **5**, 042002 (2018).
[30] M. Gibertini, M. Koperski, A. F. Morpurgo, and K. S. Novoselov, Nat. Nanotechnol. **14**, 408 (2019).
[31] K. Özdoğan, E. Şaşıoğlu, and I. Galanakis, J. Appl. Phys. **113**, 193903 (2013).
[32] S. V. Faleev, Y. Ferrante, J. Jeong, M. G. Samant, B. Jones, and S. S. P. Parkin, Phys. Rev. Mater. **1**, 024402 (2017).
[33] T. Graf, C. Felser, and S. S. P. Parkin, Prog. Solid State Chem. **39**, 1 (2011).
[34] Q. Gao, I. Opahle, and H. Zhang, Phys. Rev. Mater. **3**, 024410 (2019).
[35] T. Aull, E. Şaşıoğlu, I. V. Maznichenko, S. Ostanin, A. Ernst, I. Mertig, and I. Galanakis, Phys. Rev. Mater. **3**, 124415 (2019).
[36] W. Rotjanapittayakul, J. Prasongkit, I. Rungger, S. Sanvito, W. Pijitrojana, and T. Archer, Phys. Rev. B **98**, 054425 (2018).
[37] B. Radisavljevic, A. Radenovic, J. Brivio, V. Giacometti, and A. Kis, Nat. Nanotechnol. **6**, 147 (2011).
[38] L. Li, Y. Yu, G. J. Ye, Q. Ge, X. Ou, H. Wu, D. Feng, X. H. Chen, and Y. Zhang, Nat. Nanotechnol. **9**, 372 (2014).
[39] D. Jariwala, V. K. Sangwan, L. J. Lauhon, T. J. Marks, and M. C. Hersam, ACS Nano **8**, 1102 (2014).
[40] G. Fiori, F. Bonaccorso, G. Iannaccone, T. Palacios, D. Neumaier, A. Seabaugh, S. K. Banerjee, and L. Colombo, Nat. Nanotechnol. **9**, 768 (2014).
[41] T. Roy, M. Tosun, X. Cao, H. Fang, D.-H. Lien, P. Zhao, Y.-Z. Chen, Y.-L. Chueh, J. Guo, and A. Javey, ACS

Nano **9**, 2071 (2015).
[42] Y. Liu, N. O. Weiss, X. Duan, H.-C. Cheng, Y. Huang, and X. Duan, Nat. Rev. Mater. **1**, 16042 (2016).
[43] R. Yan, S. Fathipour, Y. Han, B. Song, S. Xiao, M. Li, N. Ma, V. Protasenko, D. A. Muller, D. Jena, et al., Nano Lett. **15**, 5791 (2015).
[44] F. Giannazzo, G. Greco, F. Roccaforte, and S. S. Sonde, Crystals **8**, 70 (2018).
[45] M.-Y. Li, C.-H. Chen, Y. Shi, and L.-J. Li, Mater. Today **19**, 322 (2016).
[46] J. Choukroun, M. Pala, S. Fang, E. Kaxiras, and P. Dollfus, Nanotechnology **30**, 025201 (2018).
[47] H. L. Zhuang and R. G. Hennig, Phys. Rev. B **93**, 054429 (2016).
[48] N. Luo, C. Si, and W. Duan, Phys. Rev. B **95**, 205432 (2017).
[49] H.-R. Fuh, C.-R. Chang, Y.-K. Wang, R. F. Evans, R. W. Chantrell, and H.-T. Jeng, Sci. Rep. **6**, 32625 (2016).
[50] D. Gao, Q. Xue, X. Mao, W. Wang, Q. Xu, and D. Xue, J. Mater. Chem. C **1**, 5909 (2013).
[51] M. Bonilla, S. Kolekar, Y. Ma, H. C. Diaz, V. Kalappattil, R. Das, T. Eggers, H. R. Gutierrez, M.-H. Phan, and M. Batzill, Nat. Nanotechnol. **13**, 289 (2018).
[52] G. H. Han, D. L. Duong, D. H. Keum, S. J. Yun, and Y. H. Lee, Chem. Rev. **118**, 6297 (2018).
[53] S. Smidstrup, D. Stradi, J. Wellendorff, P. A. Khomyakov, U. G. Vej-Hansen, M.-E. Lee, T. Ghosh, E. Jónsson, H. Jónsson, and K. Stokbro, Phys. Rev. B **96**, 195309 (2017).
[54] J. P. Perdew, K. Burke, and M. Ernzerhof, Phys. Rev. Lett. **77**, 3865 (1996).
[55] M. J. Van Setten, M. Giantomassi, E. Bousquet, M. J. Verstraete, D. R. Hamann, X. Gonze, and G.-M. Rignanese, Comput. Phys. Commun. **226**, 39 (2018).
[56] S. Smidstrup, T. Markussen, P. Vancraeyveld, J. Wellendorff, J. Schneider, T. Gunst, B. Verstichel, D. Stradi, P. A. Khomyakov, U. G. Vej-Hansen, et al., J. Phys. Condens. Matter **32**, 015901 (2019).
[57] M. Büttiker, Y. Imry, R. Landauer, and S. Pinhas, Phys. Rev. B **31**, 6207 (1985).
[58] C. Jiang, Y. Wang, Y. Zhang, H. Wang, Q. Chen, and J. Wan, J. Phys. Chem. C **122**, 21617 (2018).
[59] N. D. Mermin and H. Wagner, Phys. Rev. Lett. **17**, 1133 (1966).
[60] S. T. Bramwell and P. C. W. Holdsworth, Phys. Rev. B **49**, 8811 (1994).
[61] D. Torelli, K. S. Thygesen, and T. Olsen, 2D Mater. **6**, 045018 (2019).
[62] F. Matsukura, Y. Tokura, and H. Ohno, Nat. Nanotechnol. **10**, 209 (2015).
[63] R. O. Cherifi, V. Ivanovskaya, L. C. Phillips, A. Zobelli, I. C. Infante, E. Jacquet, V. Garcia, S. Fusil, P. R. Briddon, N. Guiblin, et al., Nat. Mater. **13**, 345 (2014).
[64] V. L. Korenev, I. V. Kalitukha, I. A. Akimov, V. F. Sapega, E. A. Zhukov, E. Kirstein, O. S. Ken, D. Kudlacik, G. Karczewski, M. Wiater, et al., Nat. Commun. **10**, 2899 (2019).
[65] C.-Y. You and S. D. Bader, J. Magn. Magn. Mater. **195**, 488 (1999).
[66] Y.-H. Tang, N. Kioussis, A. Kalitsov, W. H. Butler, and R. Car, Phys. Rev. Lett. **103**, 057206 (2009).
[67] S. Sayed, C.-H. Hsu, N. Roschewsky, S.-H. Yang, and S. Salahuddin (2019), 1911.00183.
[68] T. Newhouse-Illige, Y. Liu, M. Xu, D. Reifsnyder Hickey, A. Kundu, H. Almasi, C. Bi, X. Wang, J. W. Freeland, D. J. Keavney, et al., Nat. Commun. **8**, 15232 (2017).
[69] Z.-Q. Fan, X.-W. Jiang, J.-W. Luo, L.-Y. Jiao, R. Huang, S.-S. Li, and L.-W. Wang, Phys. Rev. B **96**, 165402 (2017).
[70] *International Roadmap for Devices and Systems (IRDS)* (2017), available at https://irds.ieee.org, URL `https://irds.ieee.org/editions/2017`.
[71] M. Shanawani, D. Masotti, and A. Costanzo, Electronics **6**, 99 (2017).
[72] S. Joshi and G. Moddel, IEEE J. Photovolt. **6**, 668 (2016).
[73] S. Grover, S. Joshi, and G. Moddel, J. Phys. D: Appl. Phys. **46**, 135106 (2013).
[74] M. I. Katsnelson, V. Y. Irkhin, L. Chioncel, A. I. Lichtenstein, and R. A. de Groot, Rev. Mod. Phys. **80**, 315 (2008).